Estimation of strong ground motion in broad-frequency band based on a seismic source scaling model and an empirical Green's function technique

KOJIRO IRIKURA and KATSUHIRO KAMAE

from

ANNALI DI GEOFISICA

Vol. XXXVII, N. 6, December 1994, pp. 1721-1743

Editrice Compositori

ANNALI DI GEOFISICA, VOL. XXXVII, N. 6, December 1994

Estimation of strong ground motion in broad-frequency band based on a seismic source scaling model and an empirical Green's function technique

Kojiro Irikura ([1]) **and Katsuhiro Kamae** ([2])
([1]) *Disaster Prevention Research Institute, Kyoto University, Kyoto, Japan*
([2]) *Nuclear Reactor Research Institute, Kyoto University, Kumatori, Osaka, Japan*

Abstract
We introduce a generalized method for simulating strong ground motion from large earthquakes by summing subevent records to follow the ω^2 law. The original idea of the method is based on a constant stress parameter between the target event and the subevent. It is applicable to a case where both events have a different stress drop after some manipulation. However, the simulation for a very large earthquake from a small event with this method has inevitably some deficiencies of spectral amplitudes in the intermediate frequency range deviating from the ω^2 model, although the high and low frequency motions match the scaling. We improve the simulation algorithm so as not to make spectral sags, introducing self-similar distribution of subfaults with different sizes in the fault plane, so-called fractal composite faulting model. We show successful simulations for intermediate-sized earthquakes (M_{JMA} = 5.0, 6.0 and 6.1), the large aftershocks of the 1983 Akita-Oki earthquake, using the records of smaller aftershocks (M_{JMA} = 3.9 and 5.0) as an empirical Green's function. Further, we attempted to estimate strong ground motion for the 1946 Nankai earthquake with M_w 8.2, using the records of a M_{JMA} 5.1 earthquake occurring near the source region of the mainshock. We found that strong ground motions simulated for the fractal composite faulting model with two asperities radiating significantly high frequency motions matched well the observed data such as the near-field displacement record, the source spectrum estimated from the teleseismic record, and the seismic intensity distribution during the 1946 Nankai earthquake.

Key words *empirical Green's function – strong ground motion – scaling law*

1. Introduction

Accurate estimation of strong motion waveform in a broad-frequency band is indispensable to establishing the recent technology of the earthquake-resistant design and response-controlled design of structure to reduce earthquake damage. However, it is still difficult to calculate Green's function theoretically in a broad-frequency band for realistic complex media. The reason is that we cannot obtain geophysical and geotechnical information on propagation-paths from source to site exactly enough for the numerical calculation of Green's function, although the calculation techniques for the 3-D and computer abilities have been developed.

A useful approach for this purpose is to estimate strong ground motion for a large earthquake using the records of small earthquakes, considered as an empirical Green's function (Hartzell, 1978). The frequency range available for simulations in this method depends on the signal-to-noise ratios of weak motion records from small events and it has been limited to frequencies higher than 0.5 Hz for conventional strong-motion-accelerograms from less

than magnitude 5, for example. Fortunately recent instruments for measuring strong ground motion have provided wide dynamic range data in broad-frequency band from several hundredths to several tens Hz.

The original idea of the empirical Green's function method comes from the use of the records of small events instead of the theoretical Green's function. From the above point of view, it is desirable that the small events should be as small as possible to be able to assume a point source solution in fault size. However, most successful simulations with the empirical Green's function method have been made using not so small events as compared to the target events. To simulate strong ground motions from very large earthquakes using the records of a small event, the fault area of the target event is divided into a large number of identical subfaults whose size coincides with the small-event fault area. Then, some deficiencies of synthetic spectra are inevitably produced even if the small event records are accurate enough in broad-frequency band, similar to the procedure of Joyner and Boore (1986). To avoid such spectral deficiencies, we introduce a fractal distribution of a set of subfaults with different sizes in the fault area in simulating large earthquake motions.

In this paper, we show first the simulation tests for intermediate-sized events, the large aftershocks (M_{JMA} = 6.1, 6.0, and 5.0) of the 1983 Akita-Oki earthquake using smaller aftershocks as empirical Green's functions (M_{JMA} is a seismic magnitude determined by the Japan Meteorological Agency). Next, the simulation for very large events is examined. Strong ground motion for the 1946 Nankai earthquake with moment magnitude (M_w) 8.2 are estimated using the records of a small event with M_{JMA} 5.1. By comparing the simulation results and the observed data, we discuss the physical basis of our simulation procedure.

2. Methodology for the empirical Green's function method

We outline the estimation method of strong ground motion from a large earthquake based on the similarity law of earthquakes and the idea of an empirical Green's function put forward by Irikura (1986).

2.1. *Similarity relationships of earthquakes*

There are considered two similarity relations between large and small earthquakes. One is the scaling relations of source parameters such as fault area, slip and slip duration, and the other is the scaling relations of source spectra.

The scaling of the source parameters studied by Kanamori and Anderson (1975) are given as

$$L/l = W/w = T/\tau = (M_0/m_0)^{1/3} = N, D/d = N, \tag{2.1}$$

where, for large and small events, L and l are fault length, W and w are width, T and τ are slip duration time, M_0 and m_0 are seismic moment, and D and d are fault slip respectively. This scaling is based on the idea of size-independent stress drop, as static stress drop is proportional to $M_0/(LW)^{3/2}$ [equal to $m_0/(lw)^{3/2}$]. Under the above conditions, when the fault area of the target event is divided into $N \times N$ subfaults, the area of each subfaults coincide with that of the small event.

The other scaling, so-called the ω^2 spectral scaling model, was studied by Aki (1967) and Brune (1970). This model has been considered a useful reference model even for great earthquakes (Houston and Kanamori, 1986) as well as intermediate-sized earthquakes (Hanks and McGuire, 1981). The shape of the ω^2 source spectrum $\tilde{U}$, regardless of the earthquake size, is given by

$$\tilde{U}(f) = \tilde{U}_0/[1 + (f/f_c)^2] \tag{2.2}$$

where spectral corner frequency f_c and the low-frequency ($f < f_c$) level $\tilde{U}_0$ are proportional to the inverse of the fault dimension $(LW)^{-1}$ and the seismic moment M_0, respectively. Then, the average stress drop is proportional to $M_0 f_c^3$. If

the average stress drop is independent of M_0, self-similarity exists among earthquakes (Aki, 1967). Then the corner frequency is proportional to M_0^{-3} and the high-frequency ($f > f_c$) acceleration flat-level $\tilde{A}_0$ is proportional to $M_0^{1/3}$ as shown in fig. 1a,b. Therefore, the spectral relationship between large and small events is as follows:

$$\tilde{U}_0/\tilde{u}_0 = M_0/m_0 = N^3, \tilde{A}_0/\tilde{a}_0 = (M_0/m_0)^{1/3} = N, \quad (2.3)$$

where $\tilde{U}_0$ and $\tilde{u}_0$ are the flat level of the displacement spectrum, $\tilde{A}_0$ and $\tilde{a}_0$ are that of the acceleration spectrum, for large and small events, respectively.

The failure of self-similarity for very large earthquakes more than $M_w = 8.25$ is indicated by Hartzell and Heaton (1988), because the rupture width for such large earthquakes reaches the uppermost mantle with significant rheological differences. In other words, the ω^2 scaling model is useful up to very large earthquakes with $M_w = 8.25$.

One problem comes from the observational fact that the condition of constant stress drop does not always hold in wide magnitude range. Therefore, we need to introduce a small flexible condition for the ω^2 model, having the shape of the ω^2 source spectrum, but not constant stress drop. Then, the spectral relationships between large and small earthquakes (2.3) are changed as follows.

$$\tilde{U}_0/\tilde{u}_0 = M_0/m_0 = CN^3, \tilde{A}_0/\tilde{a}_0 = CN, \quad (2.4)$$

where C is the stress drop ratio between both events. The scaling of source parameters (2.1) is also necessarily modified to be

$$L/l = W/w = T/\tau = [M_0/(C m_0)]^{1/3} = N,$$
$$D/d = CN. \quad (2.5)$$

The algorithm simulating strong ground motion from a large earthquake has to be made to satisfy the above two scaling relations (2.1) and (2.3), or (2.5) and (2.4).

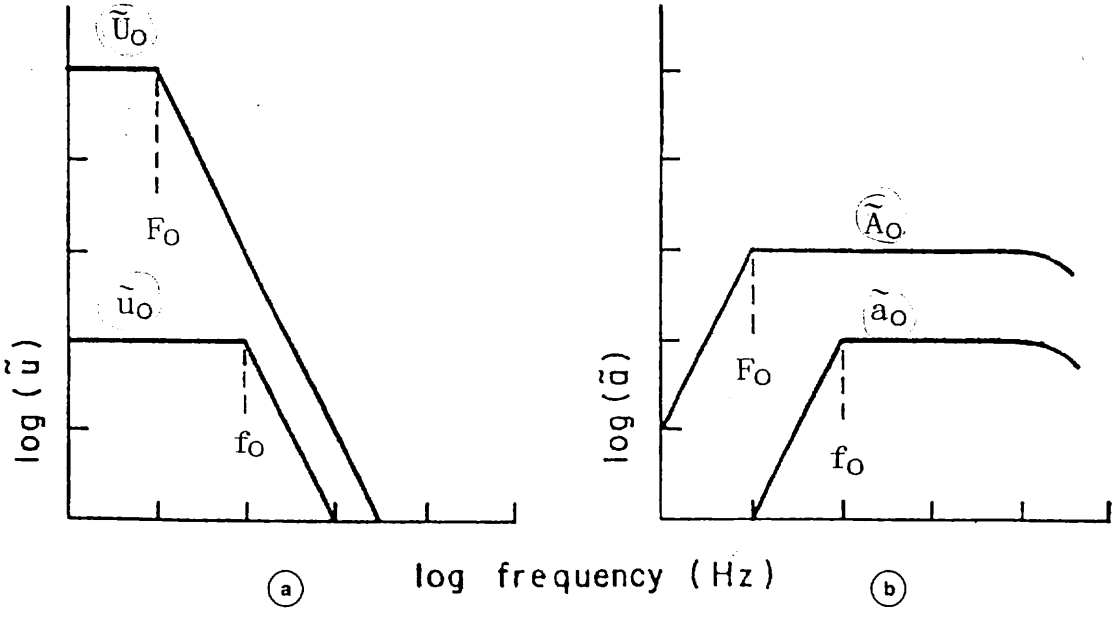

Fig. 1a,b. Theoretical displacement (a) and acceleration (b) source spectra for different-sized events predicted by the ω^2 spectral scaling model with constant stress drop. For large and small events, respectively, $\tilde{U}_0$ and $\tilde{u}_0$ are the flat level of the displacement spectrum at low frequencies, F_0 and f_0 are corner frequency, and $\tilde{A}_0$ and $\tilde{a}_0$ are the flat level of the acceleration spectrum at high frequencies between the corner frequency and cut-off frequency (f_{max}).

2.2. *Simulation algorithm for the ω^2 scaling model*

The schematic illustration is shown in fig. 2a for simulating strong ground motion from a large earthquake using the records of a small event as empirical Green's functions. For simplification, here we assume the ω^2 scaling model with constant stress drop between the target event and the small event, *i.e.* $C = 1$ in (2.4). For the case of not constant stress drop, we will describe a modified method for the simulation later.

Let the moment of the target event be N^3 times that of the small events. We divide the fault plane into $N \times N$ subfaults. Then the subfault size is equivalent to the small event (hence-forth called subevent). The seismogram $A(t)$ for the target event is expressed in terms of the seismogram $a(t)$ of the subevent as follows:

$$A(t) = \sum_{i=1}^{N^2} (r/r_i)\, F(t - t_i) * a(t), \qquad (2.6)$$

$$F(t) = \delta(t) + \frac{1}{n'} \sum_{j=1}^{(N-1)n'} \delta[t - (j-1)T/(N-1)n'], \qquad (2.7)$$

and

$$t_i = r_i/V_c + \xi_i/V_r + e_i, \qquad (2.8)$$

where r is the hypocentral distance from the observation point to the subevent, r_i is the distance from the observation point to the i-th subfault, ξ_i is the distance from the rupture nucleation point to the i-th subfault, V_r is the rupture speed, V_c is the velocity of seismic waves under consideration, T is the rise time of the target event, n' is an appropriate integer to eliminate spurious periodicity (Irikura, 1983), e_i is a random number between $-c_w/V_r$ and $+c_w/V_r$ ($0 < c < 1$) and $*$ represents the convolution. $F(t)$ is a filtering function to adjust a difference in slip time function between the target event and the subevent shown in fig. 2b.

In operating (2.6), the low frequency motions are summed coherently, the spectral amplitude of the subevent in the low frequency limit being amplified N^3 times and matching the moment of the target event. The high frequency motions, on the other hand, are summed incoherently, the high frequency spectral level of the subevent, being amplified N times (the square root of the summation number N^2), because $F(t)$ has an asymptotic spectral-level of unity at high-frequencies. Thus, the spectral amplitude ratio between the simu-

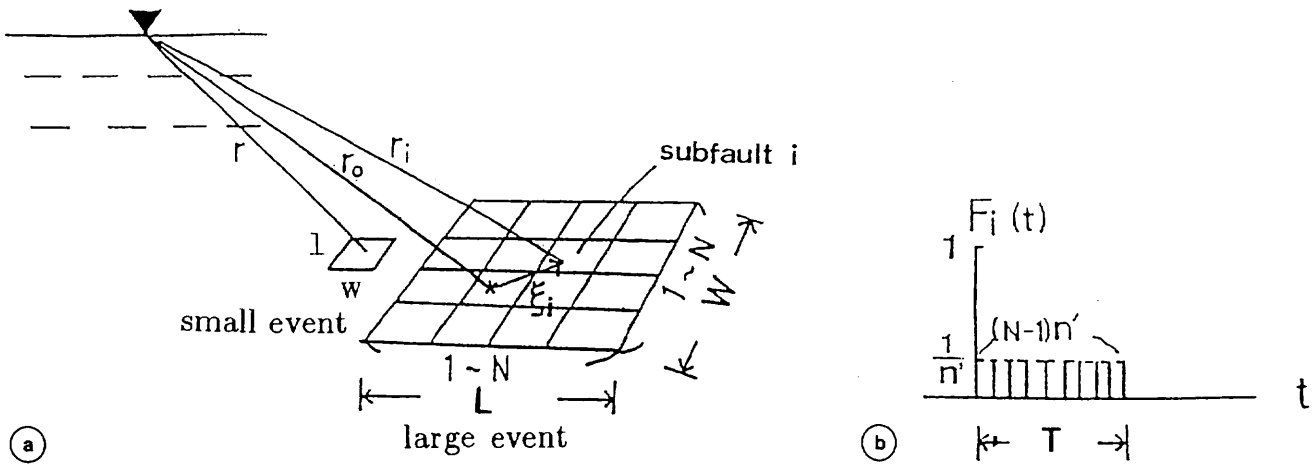

Fig. 2a,b. a) Schematic illustration of fault parameterization used for computing Green's functions. The fault areas of the large and small events are defined to be $L \times W$ and $l \times w$, respectively. b) $F_i(t)$ is a filtering function to adjust a difference in slip time function between the large and small events.

Case of different stress drop between large and small events $C = \dfrac{\Delta\sigma_L}{\Delta\sigma_S}$, $\Delta\sigma_L$ and $\Delta\sigma_S$ are stress drop for large and small events.

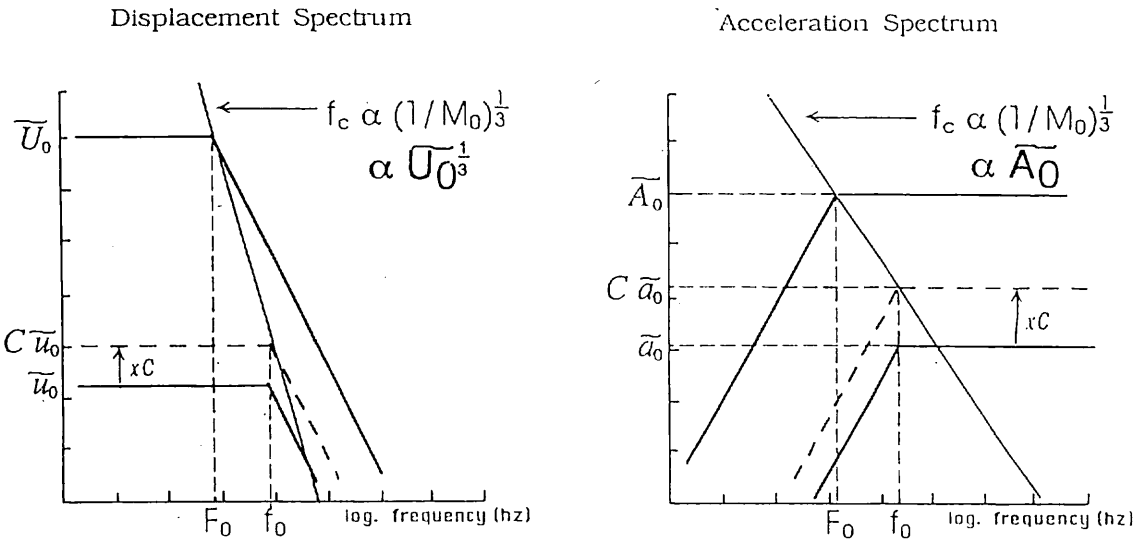

Fig. 3. Correction for a difference in stress drop between large and small events.

lated ground motion and the subevent record in the high frequency limit is proportional to the cube root of that in the low frequency limit, meeting the condition (2.3) for the ω^2 scaling law. The time-domain filter $F(t)$ described in the above equation is equivalent to the frequency-domain filter used by Boatwright (1988) for the same purpose.

The above algorithm is extended to be applicable to more general cases of source modeling, such as heterogeneous faulting models and multiple source models as shown later.

2.3. *Difference in stress drop between large and small events*

Small events occurring in the source area of the target events, do not always have the same quantity of stress drop as the target event. We assume that the source spectra of the target and small events follow the spectral shapes expected from the ω^2 model even if they have different stress drops.

Then, first the scaling parameter N and the stress drop ratio C between the target and small events are determined by solving simple equations given as (2.4) from the spectral amplitude ratios at the low-frequencies and at the high frequencies. Next, the small event record $u(t)$ is simply amplified by C. After that we can deal with the simulations in the same manner as the previous algorithm for constant stress drop by using $C\,u(t)$ instead of $u(t)$ in eq. (2.3) as illustred shown in fig. 3.

Further, we can extend this idea to an arbitrary distribution of stress drops for subfaults, if we take parameter C to vary from subfault to subfault (Irikura, 1988).

3. Simulation test-1

Simulation of intermediate-sized earthquakes (M_{JMA} 3.9 to 6.1) of the 1983 Akita-Oki earthquake sequence – We examined the applicability of the empirical Green's function method proposed here from intermediate-sized earthquakes with a JMA magnitude 3.9 to 6.1 (Yokoi and Irikura, 1991). We simulate ground motions from larger aftershocks using the records of smaller events in the 1983 Akita-

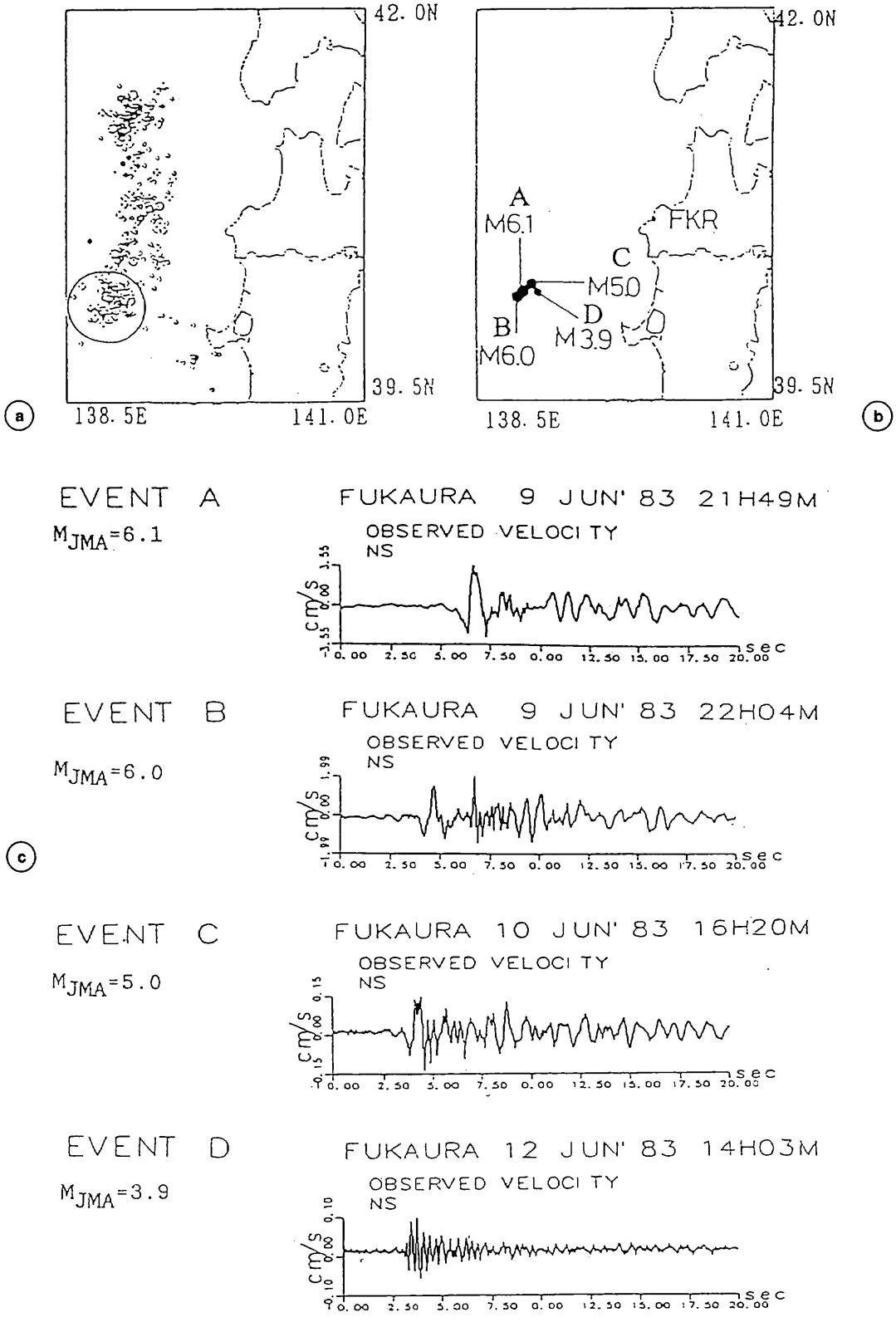

Fig. 4a-c. Epicentral distribution of aftershocks of the 1983 Akita-Oki earthquake (a), epicenters of the aftershocks (b); event A (M = 6.1), event B (M = 6.0), event C (M = 5.0), and event D (M = 3.9), analyzed in this study (Ishikawa *et al.*, 1985), and observed velocity seismograms (c), from event A with M 6.1, B with M 6.0, C with M 5.0, and D with M 3.9. The magnitude scales were determined by the Meteorological Agency.

Oki earthquake sequence (fig. 4a). We selected the records at the FKR station about 70 km from 4 aftershocks with M_{JMA} 6.1, 6.0, 5.0 and 3.9 that occurred close to each other (fig. 4b).

The moment ratios and stress drop ratios between the targets and subevents are estimated from the spectral ratios in the low frequency and high frequency range following (2.4). The source area of each event is given initially from the corner frequency using Brune's formula (1970, 1971) and finally determined as the best value from comparing between the synthetic and observed ones by forward modeling. The best parameters used for the synthetics are shown in table I.

Events A (M = 6.1), C (M = 5.0) and D (M = 3.9) are expected to be a single shock, showing simple waveforms, while event B (M = 6.0) is expected to be a multi-shock because of the complexity of its waveform. The schematic source model for simulating events A and C is shown in fig. 5. The rupture starting point is assumed to be located at the center bottom of the fault plane. The synthetic velocity of the M 5.0 event using the record of the M 3.9 event agree well with the observed one in fig. 6a, giving the scaling parameter N = 3 and the stress drop ratio C = 1. The synthetic of the M 6.1 event from the M 5.0 event also agrees well with the observed one in fig. 6b, giving N = 3 and C = 4 to correct the difference in stress drop between both events. On the other hand, as long as a single fault plane is considered, we cannot simulate the velocity waveform of the M 6.0 event to fit the observed one. A multi-event model composed of two fault segments ((3) in table I) gives us a synthetic waveform that agrees well with the observed one as shown in fig. 6c using the M 3.9 event record.

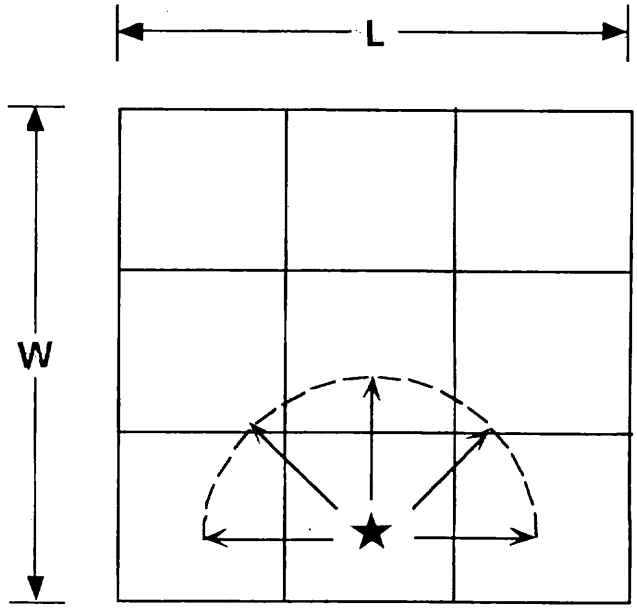

Fig. 5. Parameterization of the seismic source used for the simulations in this study. ★ Marks the rupture starting point.

4. Fractal composite model

In our previous algorithm, the fault area of the target event is divided into a number of identical subfaults. The simulated ground mo-

Table I. Parameters for simulating ground motions from large events using the records of smaller events as empirical Green's functions. (1) is the simulation for event C (M = 5.0) from event D (M = 3.9), (2) is that for event A (M = 6.1) from event C, and (3) is that for event B from event D.

		N	C	L	e	n'	V_r km/s	β km/s
(1)	C/D	3	1.0	1.5 km	0.5 km	30	3.0	3.7
(2)	A/C	3	4.0	3.3 km	1.1 km	30	3.0	3.7
(3)	B/D							
	1st	6	2.5	3.0 km	0.5 km	30	3.0	3.7
	2nd	2	10.0	1.0 km	0.5 km	30	3.0	3.7

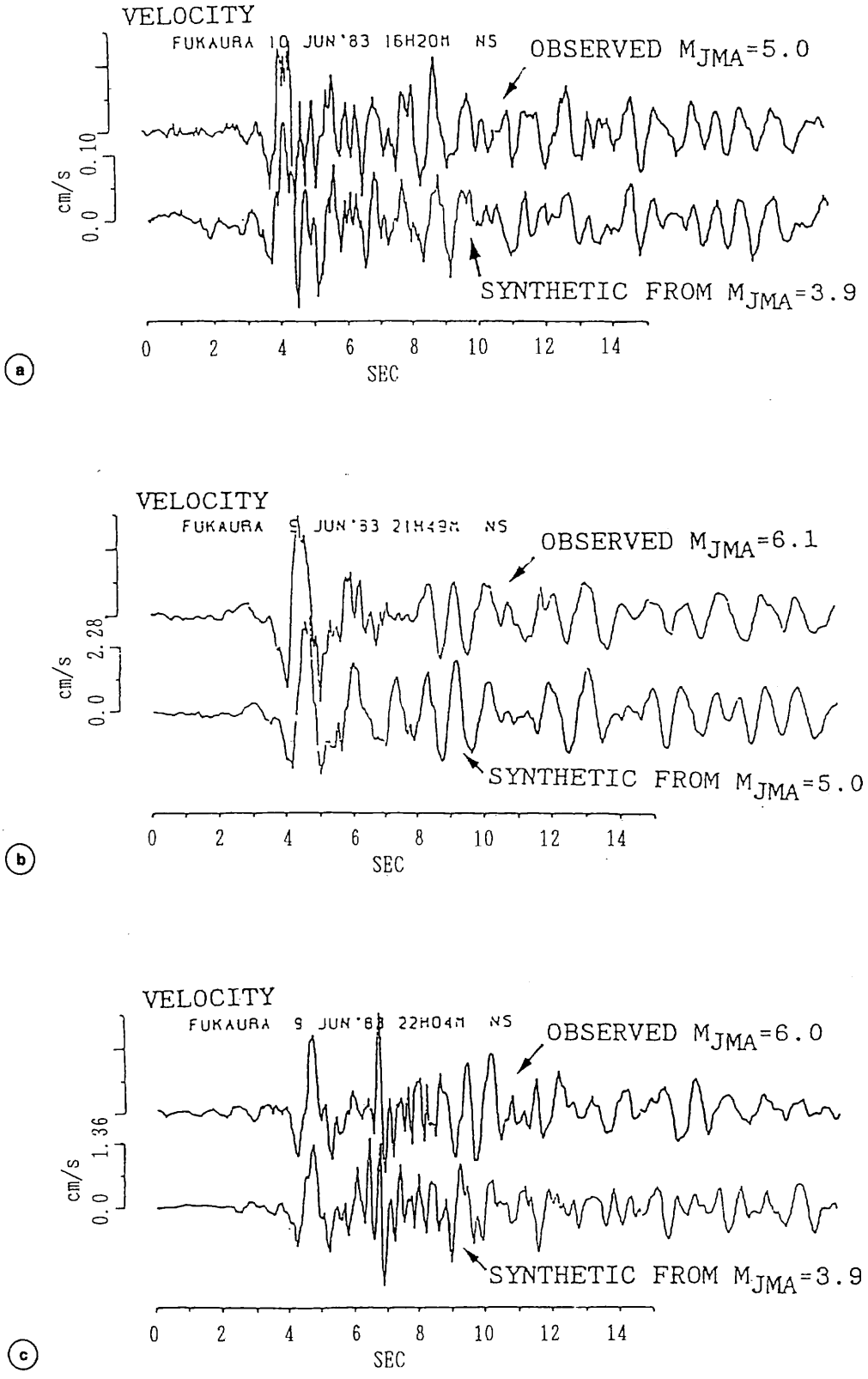

Fig. 6a-c. Comparison between observed and synthetic velocity seismograms. Event C (M = 5.0) using event D (M = 3.9) (a), event A (M = 6.1) using event C (M = 5.0) (b), and event B (M = 6.0) using event D (M = 3.9) (c), respectively, as empirical Green's functions.

tion is constrained to match the ω^2 spectrum only in the low-frequency and high-frequency limits. As long as the moment ratio between target event and subevent is less than 10^3, the simulated ground motion seems to follow the ω^2 spectrum even in the intermediate frequency range from our experiences (*e.g.* Irikura, 1986).

The results of the simulation test for different scaling factors N (moment ratio = N^3) are shown in fig. 7a-c assuming that the subevent spectrum follows the ω^2 model. For smaller scaling factor, $N = 5$, the simulated spectrum nearly follows the ω^2 model as shown in fig. 7a. However as the scaling factors increase, the simulated spectra have deeper sags in the intermediate frequency range as clearly shown in fig. 7b for $N = 25$ and fig. 7c for $N = 80$.

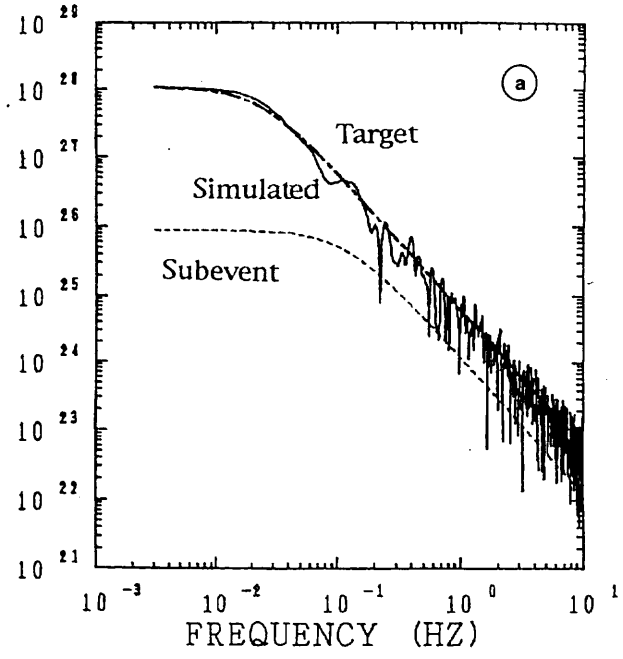

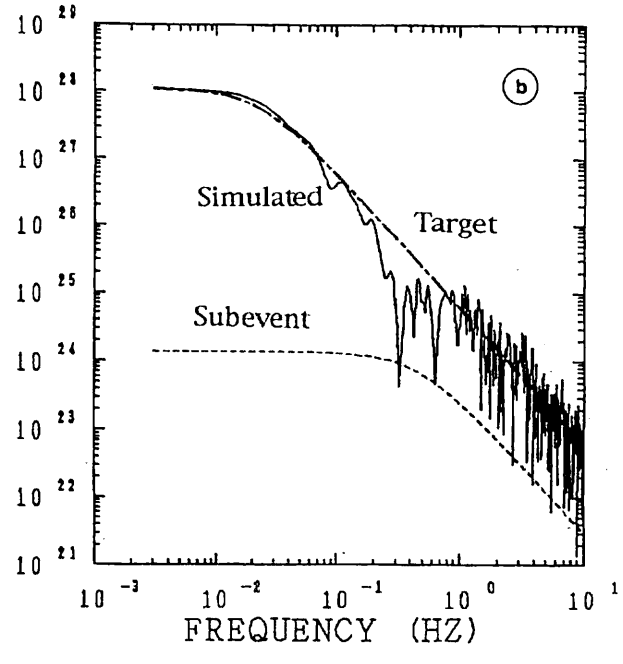

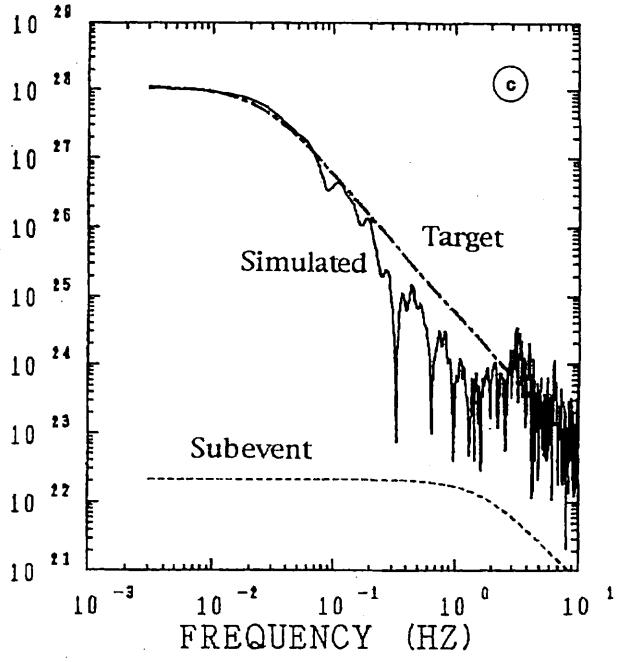

Fig. 7a-c. Simulated spectra of a target event for a difference in moment ratio between the target event and subevent, compared to the ω^2 spectrum. a) $M_0/m_0 = 5 \times 5 \times 5$; b) $M_0/m_0 = 25 \times 25 \times 25$ and c) $M_0/m_0 = 80 \times 80 \times 80$, where M_0 and m_0 are seismic moment of the target event and subevent, respectively.

To avoid such sags from the ω^2 spectrum over the intermediate frequencies, we consider that the target event has to be simulated from a set of subevents whose sizes have a fractal distribution in the total rupture area of the target event. This idea is similar to the incoherent source model by Boatwright (1982) as shown fig. 8a and the fractal source model by Frankel (1991) as shown fig. 8b, which are composed of different-sized cracks. However, a simple sum of ground motions from the subevents within the fault area does not produce the ω^2 spectral features indicated by (2.3).

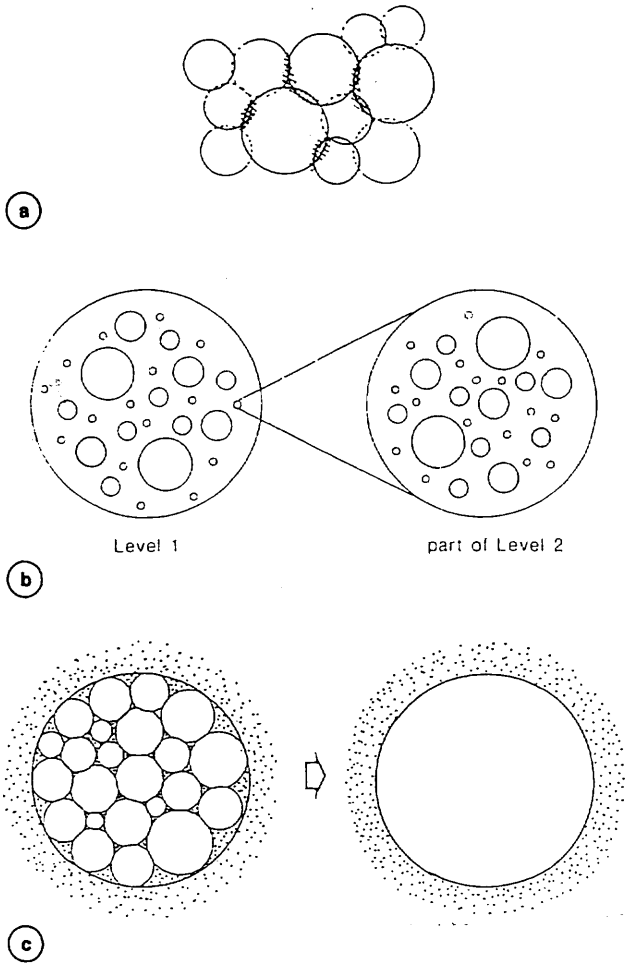

Fig. 8a-c. a) A realization of self-similar distribution of subevents for $l_0 = L/5$. l_0 is the fault diameter of the minimum sized subevent and L is the fault length of a target event after Boatwright (1982). b) Schematic illustration of self-similar distribution after Frankel (1991). c) Schematic source process of a large earthquake proposed in this study generating the ω^2 spectrum. In the initial stage, small cracks are generated and stop at barriers, and rupture goes forward skipping barriers. Eventually, barriers inside the rupture area are broken producing a large crack.

The physical basis of our algorithm for constructing a large earthquake is shown in fig. 8c. We assume that both large and small events have the ω^2 source spectra as generated by the nucleation and stopping of cracks. At the initial stage the crack-tip proceeds beyond the barriers, leaving behind unbroken barriers and making different-sized cracks distribute within a specific fault area, but the barriers between cracks eventually break due to a subsequent dynamic increase in stress (Das and Aki, 1977; Aki and Irikura, 1991). The source spectrum generated from the above process makes the ω^2 spectral shape. Our algorithm in time-domain proposed here is very similar to the frequency-domain filter used by Boatwright (1988). His idea that the ω^2 model is a composite of asperities can be equivalent to ours, since barriers in fig. 8c behave like asperities after the initial passage of the crack-tip (Aki, 1992).

The distribution of cracks, *i.e.* subevents, is assumed to be approximately self-similar to have the fractal dimension D = 2. Then, the number of different-sized subevents is given in the following procedure similar to Boatwright (1982). For simplification, we assume the fault area of the target event is a square with a length of L. The number of subevents with length greater than or equal to x occurring within the total fault area L^2 is proportional to

$$N(x) \propto L^2/x^2 . \tag{4.1}$$

Further, we assume the minimum size $l_{\min}$ and the maximum size $l_{\max}$ of the subevents. The corresponding probability density function is given as

$$n(x) = dN(x)/dx = \begin{cases} 0 & 0 < x < l_{\min} \\ kL^2/x^3 & l_{\min} < x < l_{\max} \\ 0 & l_{\max} < x < L \end{cases} \tag{4.2}$$

We consider a discrete distribution of subevents. The subevent sizes are given as x_i (i = 1, 2, - - -, m) and the number of the subevent with the size x_i is given as N_i. N_i is defined to be

$$N_i = n(x_i)\,\Delta x\,,$$
$$= (kL^2/x_i^3)\,\Delta x\,. \qquad (4.3)$$

That is, N_i is the number of the subevents with the size between x_i and $x_i + \Delta x$. The total fault area is covered by non-overlapping subevents. Then, the sum of the subevent areas is equal to the fault area of the target event

$$\sum_{i=1}^{m} x_i^2 N_i = L^2\,. \qquad (4.4)$$

From (4.2) and (4.3),

$$k = 1/\sum_{i=1}^{m}(\Delta x/x_i) \qquad (4.5)$$

and then the number of subevents with a size of x_i is given as

$$N_i = (L^2/x_i^2)/\sum_{i=1}^{m}(\Delta x/x_i) \qquad (4.6)$$

Practically, we consider a case of having only the records $a^{(1)}(t)$ from the minimum-sized subevent with a subfault length of $x_1 = l_{\min}$ and a seismic moment of m_0. First we simulate ground motions $a^{(i)}(t)$ from larger subevents with a different subfault length of x_i (i = 1, 2, - - -, m) using the minimum-sized subevent record $a^{(1)}(t)$, when the scaling factor N for each simulation (see (2.6)) is given to be $x_i/l_{\min}$. Next we divide the fault area of the target event into subfaults with different sizes x_i randomly distributed as shown in fig. 9a. The scaling factor $N^{(i)}$ for each subfault is given to be L/x_i and the filtering function $F^{(i)}$ is given replacing the scaling factor N in (2.7) by $N^{(i)}$. The number of the subfaults with a length of x_i is N_i given by (4.6). The ground motion from

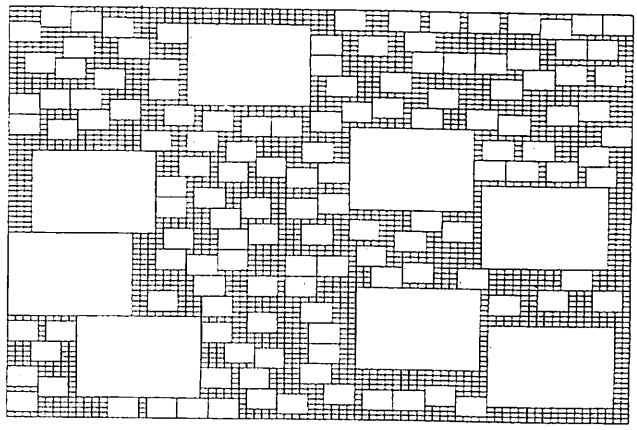

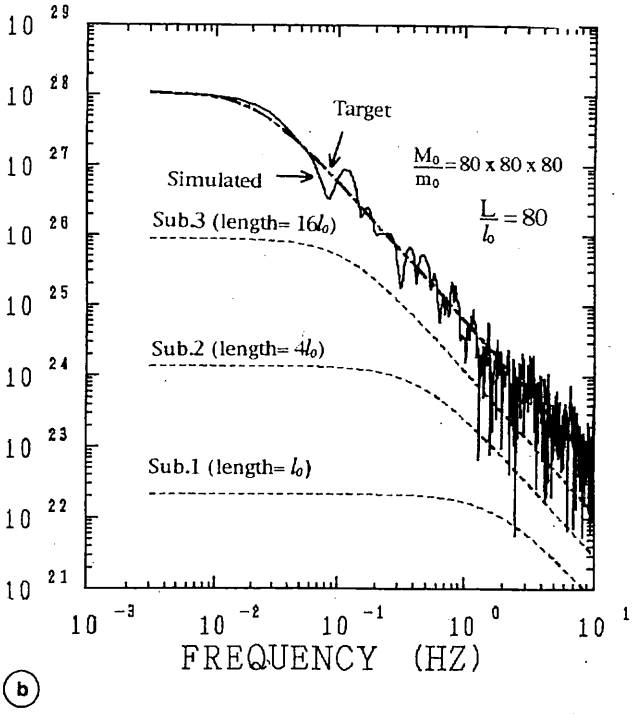

Fig. 9a,b. a) A realization of self-similar distribution of subevents composed of three different-sized subevents. b) Synthetic displacement spectrum of the target event generated from the self-similar distribution of subevents with three different sizes shown in (a), compared to the ω^2 spectrum. The spectra of three different-sized subevents are shown by dashed lines, respectively.

the p-th subfault with a length of x_i is specified as $a_p^{(i)}$, where p is numbered 1 to N_i. Then, the ground motion from the target event is obtained by superposing the ground motion $a_p^{(i)}(t)$ from all of the subfaults.

$$A(t) = \sum_{i=1}^{m} \sum_{p=1}^{N_i} (r/r_p^{(i)}) F^{(i)} * a_p^{(i)}(t - t_p^{(i)}) \,. \tag{4.7}$$

As a result, the total moment of the simulated event by (4.7) is given as

$$M_0^T = \sum_{i=1}^{m} N^{(i)} (x_i/l_{\min})^3 m_0 = \sum_{i=1}^{m} (L/x_i)(x_i/l_{\min})^3 m_0$$

$$= (L/l_{\min}^3) m_0 \sum_{i=1}^{m} x_i^2 = (L/l_{\min})^3 m_0 \,.$$

Since $(L/l_{\min})^3$ is the moment ratio between the target event and the minimum-sized subevent, the simulated ground motion by (4.7) matches the seismic moment of the target event.

The acceleration spectral level $\tilde{A}_0^T$ of the simulated ground motion is given by the power summation of the subevent acceleration spectra $\tilde{a}_{0p}^{(i)}$, because the high frequency motions from the subevents are incoherently superposed. That is,

$$(\tilde{A}_0^T)^2 = \sum_{i=1}^{m} \sum_{p=1}^{N^{(i)}} (\tilde{a}_{0p}^{(i)})^2 = \sum_{i=1}^{m} (x_i/l_{\min})^2 \tilde{a}_0^2 N_i^2$$

$$= (\tilde{a}_0/l_{\min})^2 \sum_{i=1}^{m} x_i^2 N_i^2 = (L/l_{\min})^2 \tilde{a}_0^2 \,,$$

where $\tilde{a}_0$ is the flat level of the acceleration spectrum from the minimum-sized subevent. Since $L/l_{\min}$ is equal to the scaling factor N in (2.1), the high frequency spectral-level of the simulated ground motion also matches that of the target event expected from the ω^2 model.

The spectrum simulated by the above procedure is shown in fig. 9b, in which the moment ratio between the target event and the minimum-sized subevent is given $80 \times 80 \times 80$. We find that this revised algorithm removes the sags of spectral amplitudes seen in the case of identical subfaults.

5. Simulation test-2

Simulation of the 1946 great Nankai earthquake (M_w 8.2) – Great Nankai earthquakes have occurred at a repeat time of about 100 years in the subduction zone, the Nankai Trough of South-Western Japan. The last one occurred in the region from south-off Kii-Peninsula to south-off Shikoku island as shown in fig. 10. The fault model of this earthquake has been studied using long-period surface waves (Kanamori, 1972), coseismic geodetic data and coastal geomorphic features (Ando, 1982), and the Tsunami data (Aida, 1981). Source parameters for different fault models of this event are shown in table II. The aftershock activity continued about 10 years after the mainshock, but there was very little seismic activity after that. An intermediate-sized earthquake with M_{JMA} 5.1 occurred in 1991 off Shirahama, Wakayama Prefecture, near the aftershock area of the 1946 mainshock. This event was recorded at more than 10 JMA stations with the JMA-87 strong motion accelerometers ranging from 30 to 300 km. We also obtained strong motion velocity records at WKY about 64 km away from the epicenter. We had a good opportunity to study strong ground motion during the 1946 Nankai earthquake using the records of the M_{JMA} 5.1 event as the empirical Green's function.

To check the validity of the simulations, we can analyze the following three kinds of seismic data concerning the strong ground motions during the 1946 Nankai earthquake.

Data-set 1: one horizontal-component (EW) displacement record obtained by the low-magnification (2 times) JMA displacement seismometer at SMT about 100 km from the epicenter. The digitization and careful instrumental correction of this record was made by Inoue and Matsumoto (1988).

Data-set 2: the source amplitude spectrum of this earthquake estimated by Hartzell and Heaton (1985) with the inversion analysis sep-

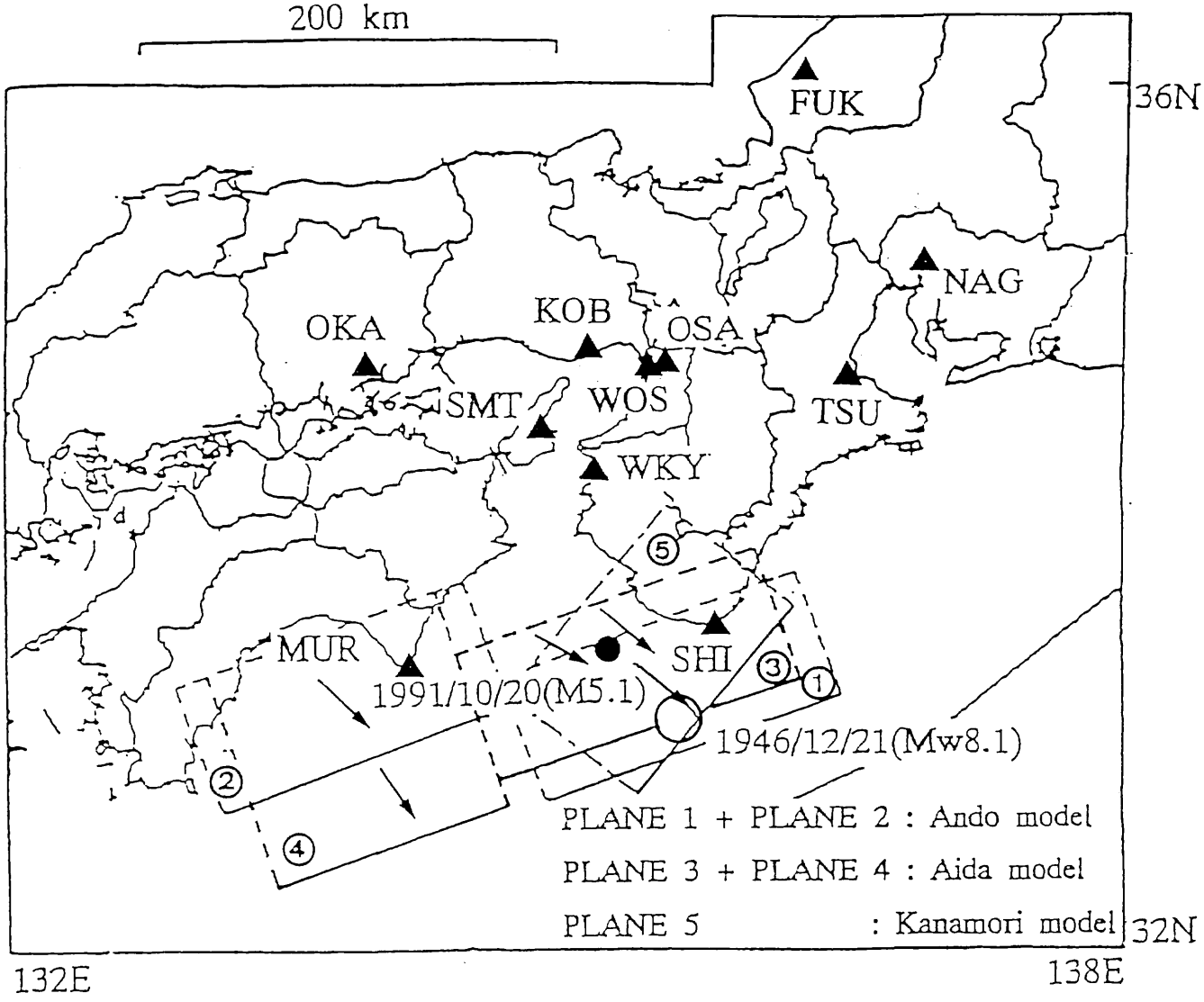

Fig. 10. Map showing the fault planes for the 1946 Nankai earthquake determined by Kanamori (1972), plane 5, Ando (1982), planes 1 and 2, and Aida (1981), planes 3 and 4. Displacement record (EW component) from this earthquake was obtained at SMT. The epicenter of the 1991 Shirahama-Oki earthquake ($M_{JMA} = 5.1$) is shown by a solid circle. Recording stations are shown by solid triangles. At SMT, where the displacement record from the 1946 Nankai earthquake was recorded, the JMA strong motion accelerograph had not yet been set up.

arating the path and site effects from the teleseismic data in Pasadena, California, Benioff 1-90 seismometer.

Data-set 3: the JMA intensity distribution during this earthquake. The peak ground accelerations and velocities at the JMA observation stations are estimated from the empirical relations by Hachimine (1989).

The seismic moment and focal mechanism of the 1991 Shirahama-Oki earthquake are reported as the CMT solutions by Dziewonski *et al.* (1992). We also estimated the seismic moment and the corner frequency from the source spectrum obtained after summing vectorially the spectral amplitude of the horizontal two components of the strong motion velocity records at WKY and correcting the propagation-path effects, as shown in fig. 11.

As the spectral shape follows the ω^2 model, the moment is estimated from the low frequency flat level and the fault area is from

Table II. Source parameters for three fault models of the 1946 Nankai earthquake (Kanamori, 1972; Aida, 1981 and Ando, 1982).

	Kanamori	Ando	Aida
L (km)	⑤ 120	① 150 ② 150	③ 150 ④ 120
W (km)	⑤ 80	① 70 ② 70	③ 70 ④ 120
M_0 (dyne-cm)	1.5×10^{28}	4.7×10^{28}	6.0×10^{28}
θ (degree)	⑤ 220	① 250 ② 250	③ 250 ④ 250
δ (degree)	⑤ 10	① 25 ② 20	③ 10 ④ 20
λ (degree)	⑤ 90	① 117 ② 117	③ 127 ④ 104
$\Delta\sigma$ (bar)	⑤ 39	① 29 ② 55	③ 48 ④ 51
τ (s)		3	
V_s (km/s)		3.5	
V_p (km/s)		2.5	

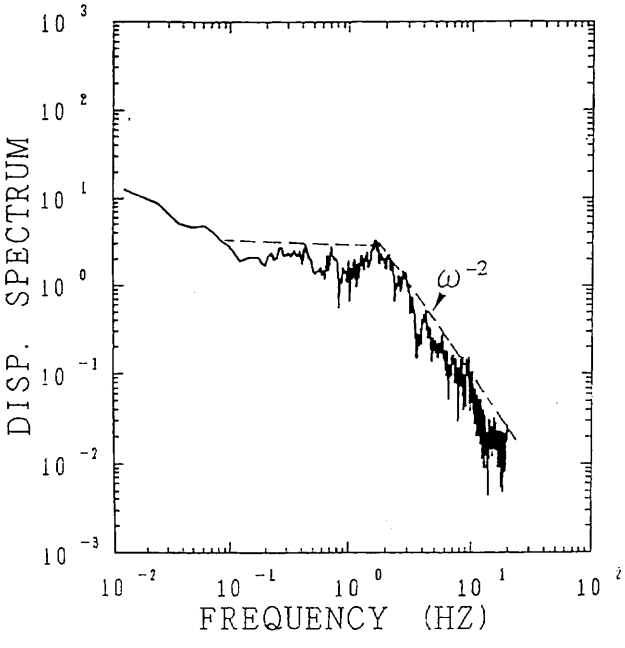

Fig. 11. The source spectrum of the 1991 Shirahama-Oki earthquake estimated by the vectorial summation of horizontal two-components recorded at WKY, where velocity-type strong motion seismometers are put on outcropped rock, compared to the ω^2 spectrum (broken line).

Brune's formula (1970) using the corner frequency from intersection between the flat level and the ω^2 decay at high frequencies. The fault mechanism is given by the distribution of P-waves first motions obtained by the local seismic-network belonging to the University of Tokyo (Nakamura, 1992). The source parameters obtained here are shown in table III, similar to the CMT solution.

Table III. Source parameters of the 1991 Shirahama-Oki earthquake with M_{JMA} = 5.1 estimated from the spectral shapes.

M_0 (dyne-cm)	6.0×10^{23}
f_c (Hz)	1.88
S (km^2)	1.5
θ (degree)	90
δ (degree)	40
λ (degree)	240
Δσ (bar)	800

Regarding data-set 1, unfortunately we had no records of the 1991 Shirahama-Oki earthquake at SMT where the 1946 mainshock was recorded because the JMA 87 accelerometers have not been set up at SMT yet. However, we do have the velocity records at WKY located at almost the same epicentral distance of about 100 km as SMT. Both stations are on outcropped rock having similar geological condition, although both stations are located at a distance of about 30 km from each other. So, we first compare the synthetic waveform of the mainshock at WKY using the record of the Shirahama-Oki earthquake to the observed one at SMT. Synthetic displacements for three fault models computed using (2.6) and the observed one at SMT are shown in fig. 12. We find that the two-segment fault models (Ando's and Aida's model) explain the observed waveform better than the one-segment fault model (Kanamori's model).

Next, we simulated the source displacement spectrum of the 1946 Nankai earthquake for the Kanamori's model using the fractal composite model in fig. 9a as shown in the upper part of the fig. 13. The observed source spectrum estimated by Hartzell and Heaton, *i.e.* data-set 2, are shown in the lower figure of fig. 13. The synthetic source spectrum has a corner frequency around 0.025 Hz clearly lower than the observed one around 0.07 Hz. According to Hartzell and Heaton (1985), the observed spectrum is resolvable in the period range from 2 to 50 s (frequency: 0.02 to 0.5 Hz), therefore the difference between the simulated and observed ones is significant. Even if we adopt the other two models (Ando's and Aida's model), the synthetic spectra are not so different from the result of Kanamori's model in fig. 13.

To fit the simulated to the observed one, we considered a heterogeneous fault model having two strong asperities with a high stress drop of 200 bars and the rest of the faulting area with a lower stress drop of 25 bars, as shown in fig. 14, modifying Aida's model that gives a better agreement between the simulated and observed displacements in fig. 12. The locations of those two asperities are given in the

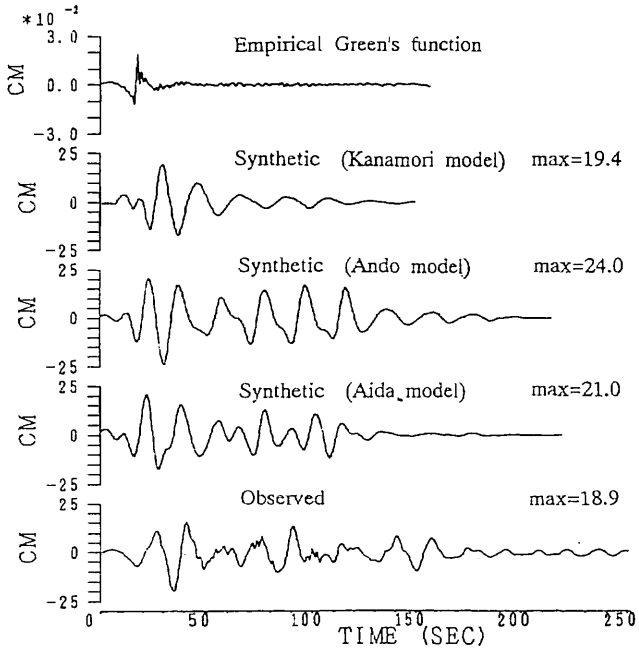

Fig. 12. Comparison of simulated displacements at WKY for three fault models (Kanamori's, Ando's and Aida's) and the observed displacement at SMT. The top trace is the EW displacement record at WKY from the 1991 Shirahama-Oki earthquake (M_{JMA} = 5.1) used as the empirical Green's function. All traces are band-pass-filtered between 0.05 and 0.5 Hz.

fault plane, referring the inversion result of geodetic and tsunami data by Satake (1993). The source spectrum simulated for the heterogeneous fault model shown in fig. 15 well fits the source spectrum (broken lines) by Hartzell and Heaton (1985). For the above heterogeneous faulting model, called here the modified Aida's model, we also computed the synthetic displacement at SMT, using the WKY record of the M 5.1 event in the same manner as the synthetic one in fig. 12 but correcting the difference in the radiation pattern effects between WKY and SMT. We found that the synthetic displacement fits well the observed one at SMT as shown in fig. 16.

We tried to check the validity of this simulation in high frequency range (1 Hz < f < 10 Hz), comparing simulated peak accelerations and velocities to estimated values from the emp-

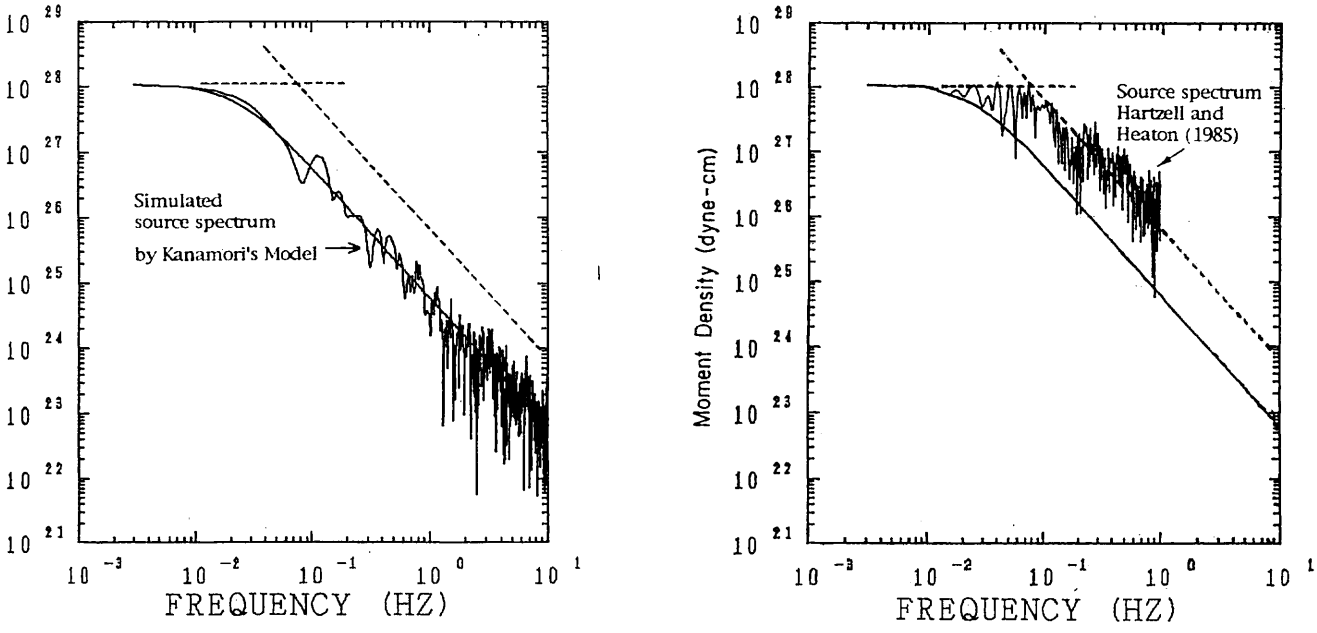

Fig. 13. Comparison of the simulated source spectrum generated by Kanamori's model and the observed source spectrum estimated from the Pasadena, California, Benioff 1-90 record by Hartzell and Heaton (1985). The dashed lines are drawn to fit the envelope of the source amplitude spectrum by Hartzell and Heaton following the ω^2 model as shown in the right figure.

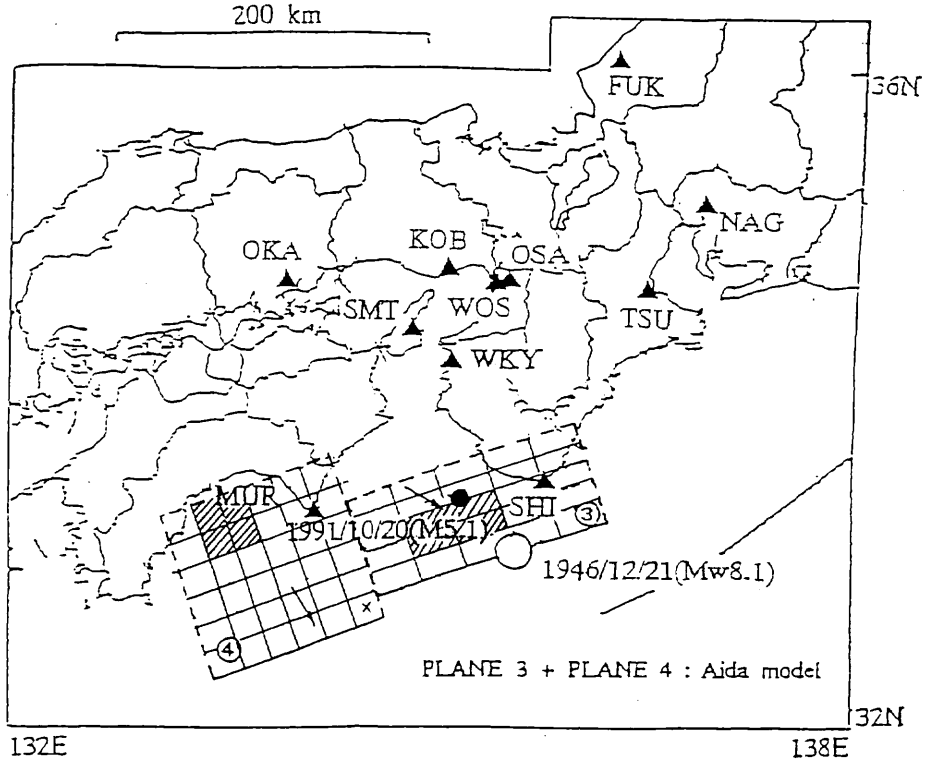

Fig. 14. Heterogeneous faulting model for the 1946 Nankai earthquake modifying Aida's model. Hatched parts are an area with a high stress drop of 200 bars, and the rest is an area with a low stress drop of 20 bars. Triangles show strong-motion stations.

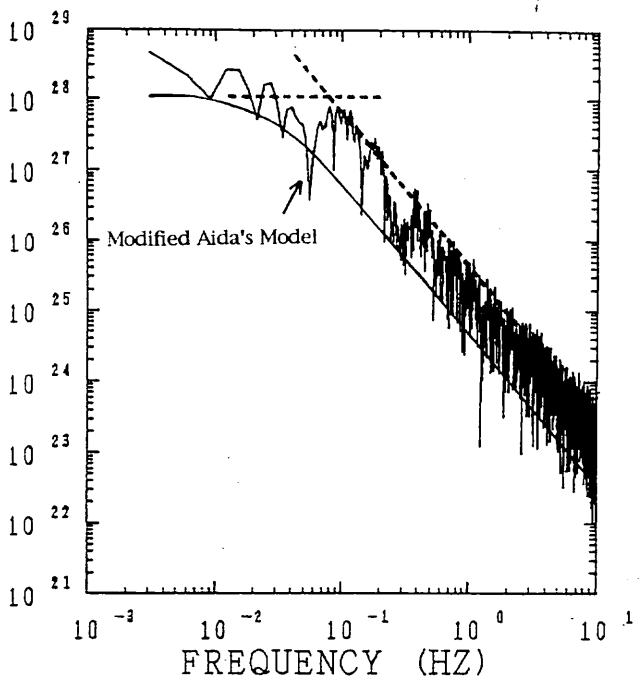

Fig. 15. Source spectrum generated by the heterogeneous fault model, compared to the source spectrum (dashed lines) estimated by Hartzell and Heaton (1985).

irical relation between the JMA intensity and peak ground acceleration and velocity in fig. 17a,b. The simulation for the heterogeneous model (Modified Aida's model) shows better agreement with the observation, than that for the uniform model (Aida's model).

We confirmed in fig. 18 that the attenuation characteristics of the observed peak ground accelerations from the 1991 Shirahama-Oki earthquake (M_{JMA} = 5.1) follow well the empirical attenuation relation from M_s 5 events occurring near Japan obtained by Fukushima and Tanaka (1990). Further, we found that the simulated peak ground accelerations from the 1946 Nankai earthquake using the records of the Shirahama-Oki earthquake also follow well the empirical attenuation relation for M_s 8.0 event equivalent to M_w 8.2, as shown in fig. 19. These facts show that this simulation method is applicable to evaluating ground motions at high frequencies even from great earthquakes with M_s 8 as long as the source processes are correctly given.

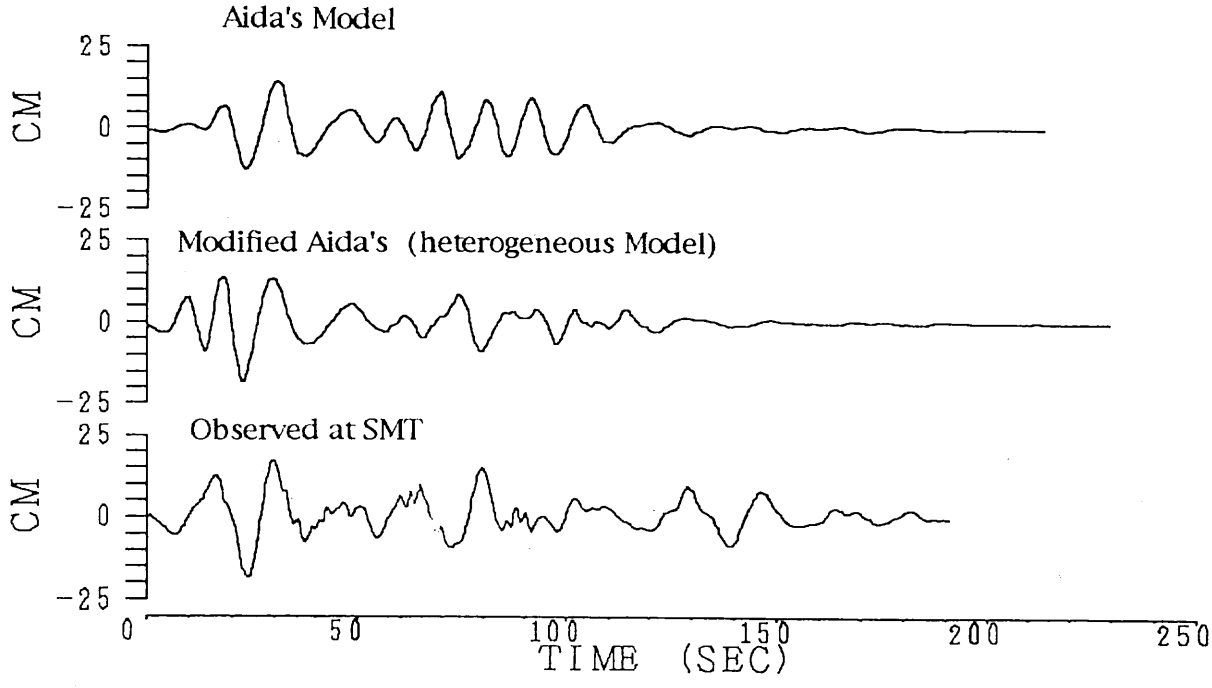

Fig. 16. Comparison of simulated displacements at SMT for the heterogeneous faulting model and the observed one. Top: Aida's model; middle: the heterogeneous faulting model (modified Aida's model); bottom: the observed displacement at SMT.

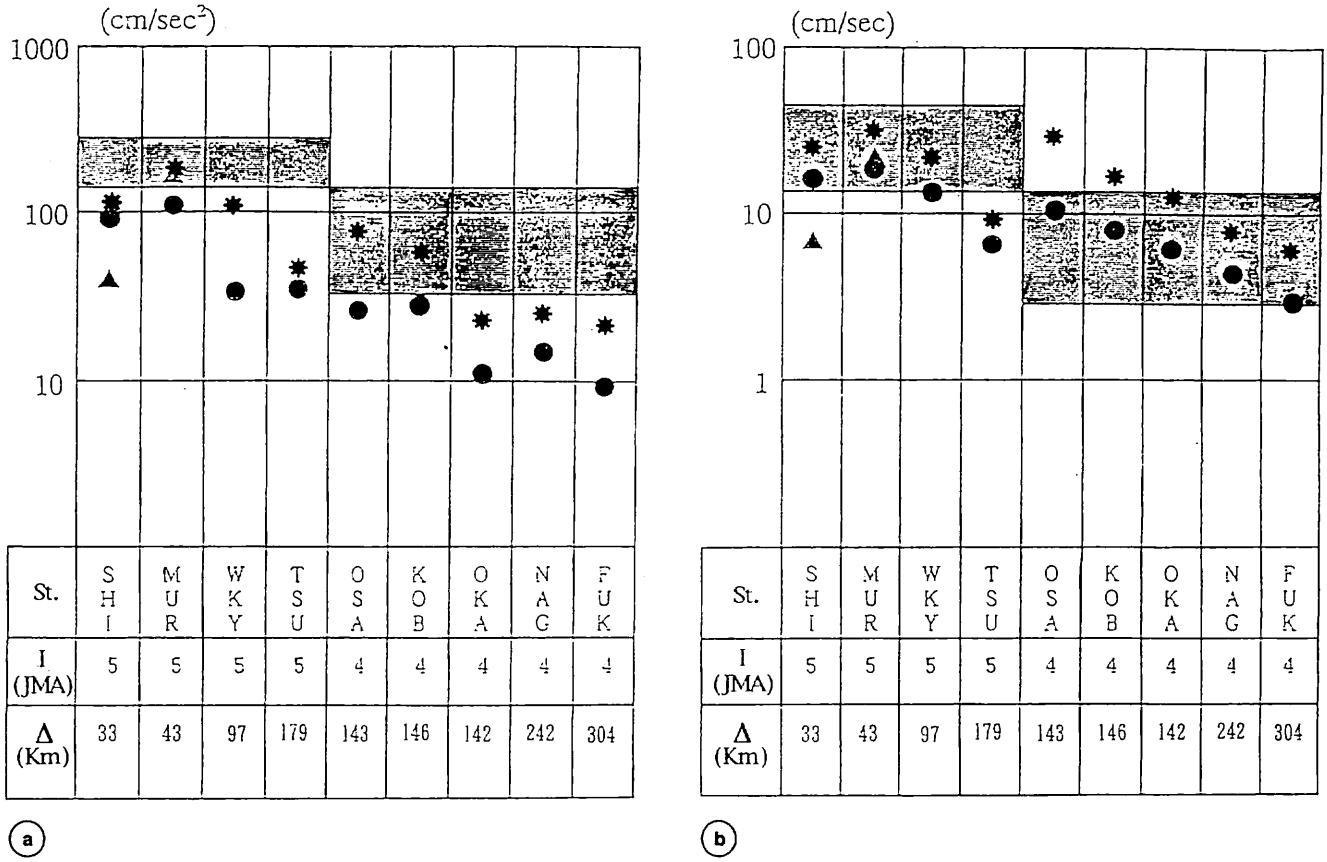

Fig. 17a,b. Comparison of peak ground accelerations (a) and velocities (b) of simulated ground motions to those estimated from the seismic intensities (JMA). Solid circles, triangles, and star marks are the peak values of the simulated ground motions for Aida's, Ando's, and the heterogeneous (modified Aida's) models, respectively. Shadows show the ranges of peak acceleration and velocity empirically evaluated from the JMA intensities.

6. Discussion and conclusions

The ground motions from large events are simulated by superimposing the records of small events in such a way as the synthetics follow the ω^2 model. The synthetics from the above method show a good fit with to the observed records of different magnitude sizes (M_{JMA} = 5.0, M 6.0, M 6.1) from about 0.1 to 10 Hz using broad-frequency band records of smaller events by velocity strong motion seismometers.

The algorithms (see (2.6)) used in this study do not sum ground motions from an aggregate of subfaults that cover the faulting area of the larger event. We cannot match both the high-frequency and low-frequency spectral amplitudes of the larger events expected from the ω^2 scaling by simply summing up small event records. Our simulation makes a summation to match not only the moment at low frequencies but also spectral contents at high frequencies to keep stress-drop constant independent of source sizes. This method can be easily extended to cases having different stress parameters between small and large events and multiple events.

The physical model to generate the ω^2 spectral scaling is a single crack model. However, as schematically shown in fig. 20a (Bernard and Madariaga, 1984), the simple crack model generates basically only two S-wave acceleration pulses (here, P-wave pulses are ignored). This is unlikely to happen during large earth-

quakes, since even in near-field observed accelerograms from large earthquakes generally do not show such simple waveforms but more complex ones. On the other hand, multiple cracks within the source area generate a number of acceleration pulses as shown in fig. 20b, but ground motions from the multi-crack source do not follow the ω^2 model. To obtain the ground motions following the ω^2 model, barriers between cracks have to be eventually broken, once cracks stop at barriers. Das and Aki (1977) had the numerical simulation in the two-dimensional problem for the above model and confirmed the seismic generation of the ω^2 model.

The physical basis of our simulation algorithm is explained by several stages as schematically shown fig. 21. When some irregularities such as barriers or asperities exist in the fault area, the crack propagation will be stopped leaving the barriers unbroken (1st stage to 4th stage in fig. 21) and eventually such barriers will be broken because of subsequent increase in dynamic stress (5th stage). For simplification, we illustrate two-dimensional cracks in fig. 21. The ground motion from three-dimensional cracks have the spectral contents expected from the ω^2 model.

We confirmed numerically that the simulation for a very large earthquake from a small event with the algorithm (2.6) has inevitably some deficiencies of spectral amplitude deviating from the ω^2 model in the intermediate frequency range, as long as the target fault area is divided into a large number of identical-sized subfaults. Then, the simulation method is improved in this study, introducing self similar distribution of subfaults with different sizes.

We tried to estimate strong ground motion for the 1946 Nankai earthquake with M_w 8.2, using the records of an M_{JMA} 5.1 event occurring near the source region of the mainshock. The amplitude spectra of the simulated ground motions by the improved method follow the ω^2

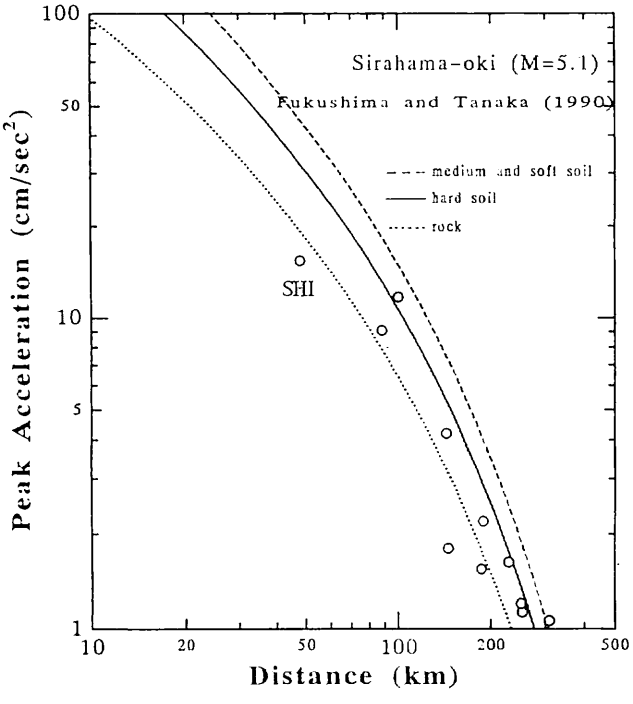

Fig. 18. Comparison of observed peak ground accelerations from the 1991 Shirahama-Oki earthquake (M_{JMA} = 5.1) and the attenuation relation for M = 5.1 by Fukushima and Tanaka (1990).

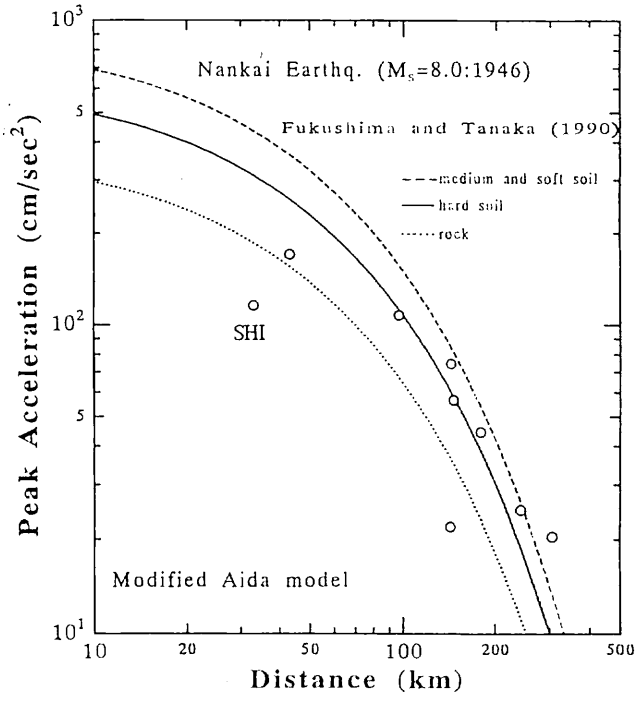

Fig. 19. Comparison of simulated peak ground accelerations for the heterogeneous fault model of the 1946 Nankai earthquake and the attenuation relation for M_s = 8.0 by Fukushima and Tanaka (1990).

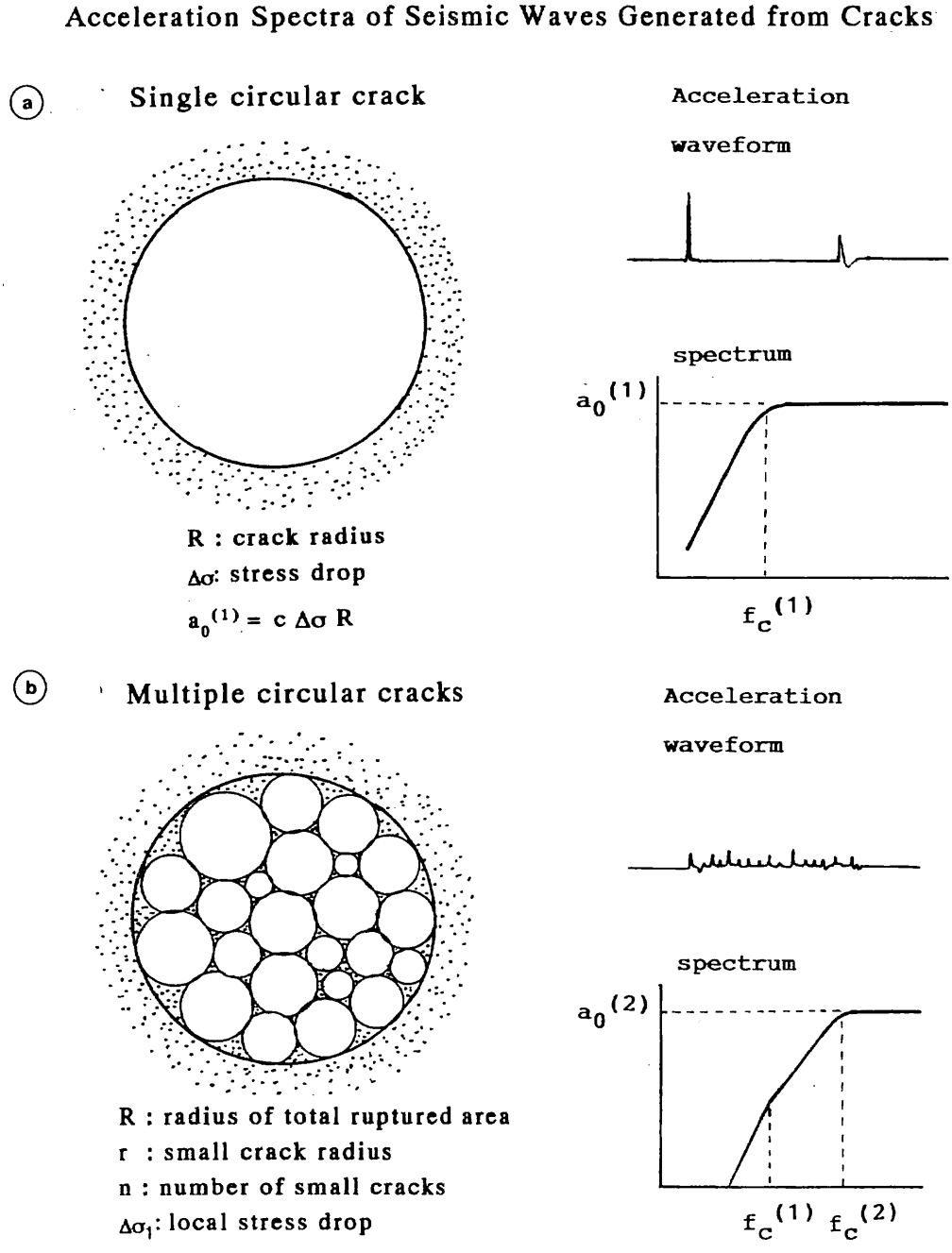

Fig. 20a,b. Illustration of source models for a large earthquake generating ground motions with the ω^2 spectral contents. Single circular-crack model (a) and multiple circular-crack model (b). In (a) and (b), the upper and lower right show the acceleration waveform and spectrum generated from respective models.

1st stage: Small cracks are generated, and each crack stops at barriers.

2nd stage: Barriers between cracks are broken, generating larger cracks.

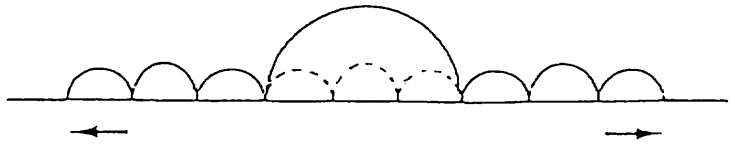

3rd stage: A larger crack sequence is generated, combining small cracks.

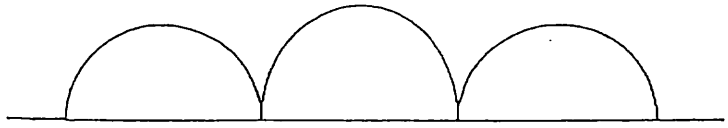

4th stage: Similar processes are going on all along the fault, increasing the size of cracks.

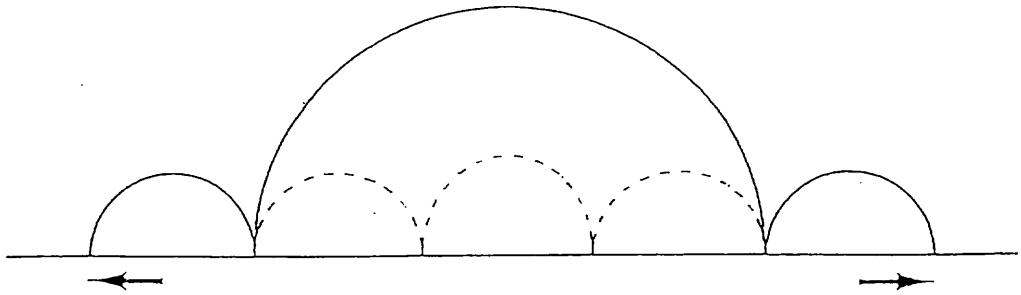

5th stage: Eventually, barriers inside the fault plane of the mainshock are all broken, producing a large crack.

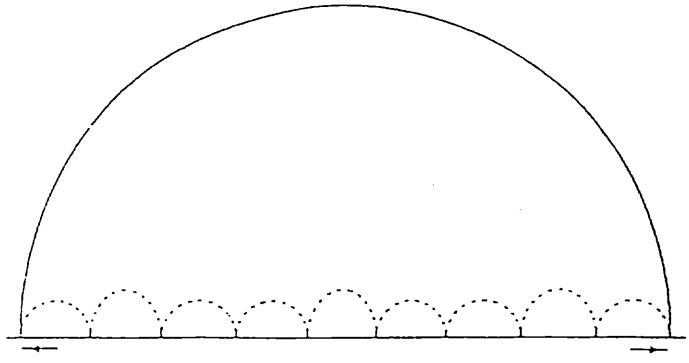

Fig. 21. Schematic explanation for the source process of a large earthquake.

model in the broad-frequency range without significant sags. However, as long as a uniform slip velocity is considered in the fault area of the mainshock inferred from the aftershock distribution and the tsunami-data, the simulated high frequency motions do not match the source amplitude spectrum estimated by Hartzell and Heaton (1985) and the peak ground accelerations estimated from the JMA intensity distribution, although the synthetic low frequency motion, *i.e.* the displacement seismogram, agrees well with the observed displacement record in the near-field. The simulation for an irregular faulting model with two asperities explains well the observed source spectrum and the estimated peak ground acceleration distributions as well as the observed displacement record in the near field.

Acknowledgements

We benefitted from the helpful comments of an anonymous reviewer. We also thank Massimo Cocco for his efforts in editing this special issue.

REFERENCES

AIDA, I. (1981): Numerical experiments for the tsunamis generated off the coast of the Nankaido district, *Bull. Earthq. Res. Inst.*, **56**, 713-730 (in Japanese with English abstract).

AKI, K. (1967): Scaling law of seismic spectrum, *J. Geophys. Res.*, **72**, 1217-1231.

AKI, K. (1992): Higher-order interrelations between seismogenic structures and earthquake processes, *Tectonophysics*, **211**, 1-12.

AKI, K. and K. IRIKURA (1991): Characterization and mapping of earthquake shaking for seismic zonation, in *Proceedings of the 4th International Conference on Seismic Zonation, Stanford, Calif.*, **I**, 61-110.

ANDO, M. (1982): A fault model of the 1946 Nankaido earthquake derived from tsunami data, *Phys. Earth Planet. Inter.*, **28**, 220-336.

BERNARD, P. and R. MADARIAGA (1984): High-frequency seismic radiation from a buried circular fault, *Geophys. J. R. Astr. Soc.*, **78**, 1-17.

BOATWRIGHT, J. (1982): The dynamic models for far-field acceleration, *Bull. Seismol. Soc. Am.*, **72**, 1049-1068.

BOATWRIGHT, J. (1988): The seismic radiation from computer models of faulting, *Bull. Seismol. Soc. Am.*, **78**, 489-508.

BRUNE, J.N. (1970): Tectonic stress and the spectra of seismic shear waves from earthquakes, *J. Geophys. Res.*, **75**, 4997-5009.

BRUNE, J.N. (1971): Tectonic stress and the spectra of seismic shear waves from earthquakes, *J. Geophys. Res.*, **76**, 5002.

DAS, S. and K. AKI (1977): Fault planes with barriers: a versatile earthquake model, *J. Geophys. Res.*, **82**, 5658-5670.

DZIEWONSKI, A.M., G. EKSTROM and M.P. SALAGANIK (1992): Centroid-moment tensor solutions for October-December 1991, *Phys. Earth Planet. Inter.*, **74**, 89-100.

FRANKEL, A. (1991): High frequency spectral falloff of earthquakes, fractal dimension of complex rupture, *b* values, and the scaling of strength on faults, *J. Geophys. Res.*, **96**, 6291-6302.

FUKUSHIMA, Y. and T. TANAKA (1990): A new attenuation relation for peak horizontal acceleration of strong earthquake ground motion in Japan. *Bull. Seismol. Soc. Am.*, **80**, 757-783.

HACHIMINE, T. (1989): On the new instrumental observation of the seismic intensity, *Q. J. Seismol.*, **52**, 43-68 (in Japanese).

HANKS, T. and R. MCGUIRE (1981): The character of high-frequency strong ground motion, *Bull. Seismol. Soc. Am.*, **71**, 2071-2095.

HARTZELL, S.H. (1978): Earthquake aftershocks as Green's functions, *Geophys. Res. Lett.*, **5**, 1-4.

HARTZELL, S.H. and T.H. HEATON (1985): Teleseismic time functions for large, shallow subduction zone earthquakes, *Bull. Seismol. Soc. Am.*, **75**, 965-1004.

HARTZELL, S.H. and T.H. HEATON (1988): Failure of self-similarity for large (M_w > 8¼) earthquakes, *Bull. Seismol. Soc. Am.*, **78**, 478-488.

HOUSTON, H. and H. KANAMORI (1986): Source spectra of great earthquakes: teleseismic constraints on rupture process and strong motion, *Bull. Seismol. Soc. Am.*, **76**, 19-42.

INOUE, R. and T. MATSUMOTO (1988): Digitization and processing of the JMA strong motion records in the period of 2 to 20 s from nine great earthquakes, *Historical Seismograms and Earthquakes of the World* (Academic Press, Inc.), 390-400.

IRIKURA, K. (1983): Semi-empirical estimation of strong ground motions during large earthquakes, *Bull. Disas. Prev. Res. Inst., Kyoto Univ.*, **33**, 63-104.

IRIKURA, K. (1986): Prediction of strong acceleration motions using empirical Green's function, in *Proceedings 7th Japan Earthquake Engineering*, 151-156.

IRIKURA, K. (1988): Estimation of near-field ground motion using empirical Green's function, in *Proceedings 9th World Conference Earthquake Engineering*, **VII**, 37-42.

ISHIKAWA, Y., K. MATSUMURA, H. YOKOYAMA and H. MATSUMOTO (1985): SEIS-PC – its outline –, *Geophys. Data Process.*, **10**, 19-34 (in Japanese).

JOYNER, W.B. and D.M. BOORE (1986): On simulating large earthquakes by Green's function addition of smaller earthquakes, in *Earthquake Source Mechanics*, edited by S. DAS and J. BOATWRIGHT, Maurice Ewing ser. 6, 269-274.

KANAMORI, H. (1972): Tectonic implications of the 1944 Tonankai and the 1946 Nankaido earthquakes, *Phys. Earth Planet. Inter.*, **5**, 129-139.

KANAMORI, H. and D.L. ANDERSON (1975): Theoretical basis of some empirical relations in seismology, *Bull. Seismol. Soc. Am.*, **65**, 1073-1095.

NAKAMURA, M. (1992): Personal communication (May 29, 1992. Wakayama Seismic Observatory, Earthquake Research Institute, University of Tokyo).

SATAKE, K. (1993): Depth distribution of coseismic slip along the Nankai Trough, Japan, from joint inversion of geodetic and tsunami data, *J. Geophys. Res.*, **98**, 4553-4565.

TAKEMURA, M. and T. IKEURA (1988): A semi-empirical method using a hybrid of stochastic and deterministic fault models: simulation of strong ground motions during large earthquakes, *J. Phys. Earth*, **36**, 89-106.

TAKEO, M. (1988): Rupture process of the 1980 Izu-Hanto-Toho-Oki earthquake deduced from strong motion seismograms, *Bull. Seismol. Soc. Am.*, **77**, 490-513.

YOKOI, T. and K. IRIKURA (1991): Empirical Green's function technique based on the scaling law of source spectra, *ZISHIN, ser. II (J. Seismol. Soc. Japan)*, **44**, 109-122 (in Japanese with English abstract).